Effect of V Content on the Microstructure and Mechanical Properties of High-Pressure Torsion Nanostructured CoCrFeMnNiV$_x$ High-Entropy Alloys

Elena. D. Tabachnikova, Sergej N. Smirnov, Yuriy O. Shapovalov, Igor V. Kolodiy, Anastasia V. Levenets, Mikhail A. Tikhonovsky, Michael J. Zehetbauer,* Christian Rentenberger, Erhard Schafler, Yi Huang, and Terence G. Langdon

The article presents investigations of microstructure and low-temperature mechanical properties of nanostructured alloys CoCrFeMnNiV$_x$ ($x = 0.15$–0.75), processed by high-pressure torsion (HPT) at temperatures of 300 and 77 K. While at $x \geq 0.5$ the values of microhardness (H_v) and compression yield stress ($\sigma_{0.2}$) in samples after HPT at 77 K are larger than those in samples after HPT at 300 K, for $x \leq 0.2$ surprisingly the opposite effect is observed. As in case of the undeformed CoCrFeMnNiV$_x$ alloys, the behavior for vanadium concentrations $x \geq 0.5$ can be related to the formation of tetragonal σ-phase in addition to face-centered cubic matrix, while the anomalous behavior for $x \leq 0.2$ arises from the formation of HPT-induced hexagonal martensitic phase. In the low-temperature ranges, i.e., 20–300 K in case of HPT nanostructured CoCrFeMnNiV$_{0.2}$, and 150–300 K in case of HPT nanostructured CoCrFeMnNiV$_{0.5}$, dependences of $\sigma_{0.2}(T)$ show characteristics of thermally activated dislocation movement. For the first time in high-entropy alloys, anomalous dependences of $\sigma_{0.2}(T)$ at temperatures 4.2–20 K for CoCrFeMnNiV$_{0.2}$, and at 80–150 K for CoCrFeMnNiV$_{0.5}$ are found, which indicate at the occurrence of nonthermal inertial dislocation movement.

1. Introduction

In recent years, there has been a significant interest in the study of the mechanical properties of a new class of materials known as high-entropy alloys (HEAs).[1–6] In the literature, the term "multicomponent concentrated alloys" is also used to designate these alloys. High values of the entropy of mixing, due to the presence of a large number of different elements in HEAs and their high concentrations, reduce the Gibbs free energy. As a result, single-phase states can form in such alloys which are in solid solution with simple crystal lattices such as face-centered cubic (fcc), body-centered cubic (bcc), or hexagonal close-packed (hcp). The most detailed studies of mechanical properties were carried out in the equiatomic single-phase fcc alloy CoCrFeMnNi (often named "Cantor alloy") which exhibits a good combination of strength, ductility, and fracture toughness at room and especially at cryogenic temperatures.[7–20,22] A further rise of strength of the CoCrFeMnNi HEA can be achieved by 1) the introduction of strengthening particles of a second phase and/or by 2) the decrease of the average grain size with a transition to an ultrafine-grained or nanostructured state. It was previously shown[22–25] that for the single-phase CoCrFeMnNi alloy, the addition of Al, V, Mo, and/or Ti favors the formation of intermetallic phases and thus the increase of strength. Stepanov et al.[23]

E. D. Tabachnikova, S. N. Smirnov, Y. O. Shapovalov
B.Verkin Institute for Low Temperature Physics and Engineering
National Academy of Sciences of Ukraine
47 Nauky Avenue, Kharkiv 61103, Ukraine

I. V. Kolodiy, A. V. Levenets, M. A. Tikhonovsky
National Science Center
Kharkiv Institute of Physics and Technology
Akademichna Street, Kharkiv 61108, Ukraine

M. J. Zehetbauer, C. Rentenberger, E. Schafler
Faculty of Physics
University of Vienna
Boltzmanngasse 5, 1090 Wien, Austria
E-mail: michael.zehetbauer@univie.ac.at

Y. Huang
Department of Design and Engineering
Faculty of Science and Technology
Bournemouth University
Poole, Dorset BH12 5BB, UK

T. G. Langdon
Department of Mechanical Engineering
University of Southampton
Southampton SO17 1BJ, UK

**ADVANCED
SCIENCE NEWS**

www.advancedsciencenews.com

**ADVANCED
ENGINEERING
MATERIALS**

www.aem-journal.com

showed that a valence electron concentration of ≈ 7.4 and an atomic radius difference of at least 3.8% of the element added are required for the formation of an intermetallic phase. All the elements mentioned, especially vanadium, fulfil that condition.

It was also established[18–20,26–29] that high-pressure torsion (HPT) processing of the single-phase HEA CoCrFeMnNi leads to nanocrystallinity and thus to a significant strengthening, too. So far, the formation of intermetallic phase and the HPT-induced nanocrystallization was not applied at the same time which, therefore, has been the task of the current work. Moreover, this investigation was designed to analyze the dependence of structure, microhardness, and mechanical properties over the temperature range of 0.5–300 K in nanostructured HEA CoCrFeMnNiV$_x$ with different concentrations of vanadium x ($x = 0.15$, 0.2, 0.3, 0.5, 0.75). The change in the structural state from coarse-grained (CG) to the nanostructured one was obtained by HPT at the two temperatures of 300 and 77 K. It is important to note that usually in ordinary metals with medium-to-high melting temperatures, a decrease in the HPT temperature leads to an increase in the values of microhardness, yield stress, and strength (see, e.g., ref. [30]). However, in the nanostructured alloy CoCrFeMnNi,[20,31–35] as well as in the nanostructured HEA Co$_{20}$Cr$_{26}$Fe$_{20}$Mn$_{20}$Ni$_{14}$,[36,37] the reduction of the HPT temperature from 300 to 77 K gave the opposite effect, i.e., a decrease in the values of these parameters compared to those obtained at 300 K. It is therefore of additional interest to analyze this effect in CoCrFeMnNiV$_x$ alloys with different concentrations of vanadium atoms.

2. Results

### 2.1. Structural Characteristics of the HPT Nanostructured Alloys

Let us first point at the dependences of shear stress $\tau(\gamma)$, and those of microhardness $H_v(\gamma)$ measured at $r \approx 2$ mm (i.e., $\gamma \approx 80$), of the samples with V-concentrations of $x \leq 0.2$ shown in Section 3.2.1 and 3.2.2, respectively: At this γ, they reach a plateau, indicating a homogeneous microstructure for sample areas at $r \geq 2$ mm. Also, for the samples with V-concentrations $x > 0.2$, only small variations of $H_v(\gamma)$ were observed for $\gamma \geq 80$. That is why all microstructural investigations described here were carried out from sample areas with $\gamma \approx 80$ corresponding to $r \approx 2$ mm.

2.1.1. XRD

At first the alloys CoCrFeMnNiV$_x$ ($x = 0.2$, 0.5, 0.75) were analyzed by methods of XRD after Cryo-HPT and RT-HPT. In **Figure 1** and **2**, the corresponding XRD patterns are given. It can be seen that after HPT at 300 and 77 K only lines of the fcc phase are visible in the diffraction patterns of the CoCrFeNiMnV$_{0.2}$ and CoCrFeNiMnV$_{0.5}$ alloys, whereas in those of the CoCrFeNiMnV$_{0.75}$ alloy there are lines of two phases corresponding to the fcc and the tetragonal σ-phase (for details of the latter, see ref. [23]). In the cast CG state, after annealing at 1000 °C the alloy CoCrFeNiMnV$_{0.25}$ is also single-phase but the diffraction pattern of the CoCrFeNiMnV$_{0.5}$ alloy already contains weak lines of the σ-phase where the volume fraction of this phase is estimated at about 28%.[23] The CoCrFeNiMnV$_{0.75}$ alloy is two-phase
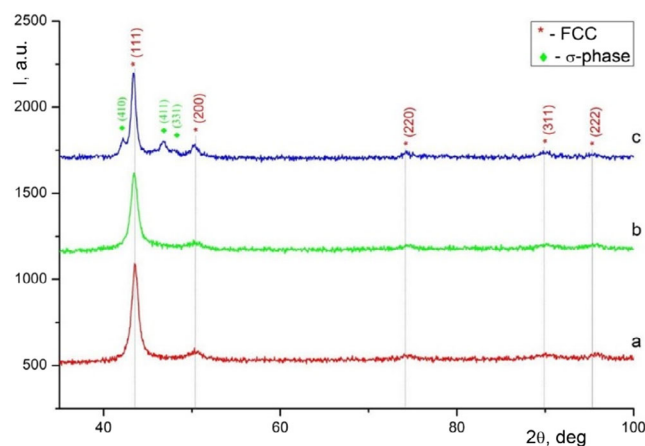
Figure 1. XRD patterns of CoCrFeMnNiV$_x$ alloy after Cryo-HPT till a torsional strain $\gamma \approx 80$: a) $x = 0.2$, b) $x = 0.5$, and c) $x = 0.75$.
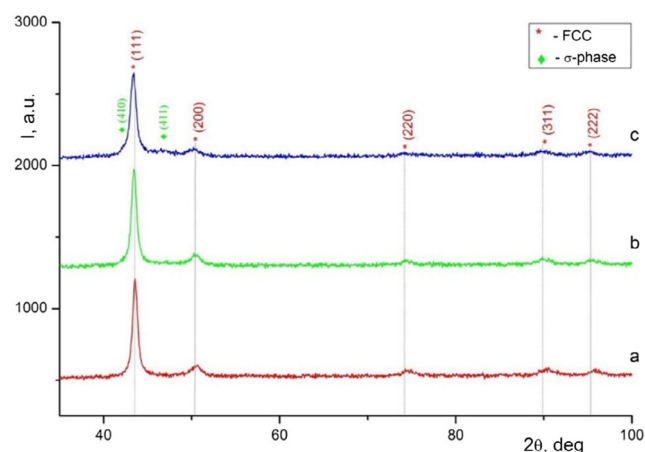
Figure 2. XRD patterns of CoCrFeMnNiV$_x$ alloy after RT-HPT till a torsional strain $\gamma \approx 80$: a) $x = 0.2$, b) $x = 0.5$, and c) $x = 0.75$.

both in the CG[23] and the HPT nanostructured state. However, the number of σ-phase diffraction lines and their intensity in the HPT nanostructured state are significantly smaller than in the CG state. Furthermore, the intensity of the σ-phase lines after Cryo-HPT is higher than after RT-HPT.

The structural characteristics of the fcc phase found in the HPT nanostructured CoCrFeMnNiV$_x$ alloy after RT-HPT and Cryo-HPT, as obtained from the relevant diffraction patterns, are given in **Table 1**. Note that in all cases there was an observed axial texture of the fcc phase with a predominant direction [111] along the axis of the disk, in which diatropic crystallographic plane grains (111) were mainly oriented parallel to the disc surfaces.

From the XRD data presented in Table 1, it follows that in the investigated HPT nanostructured alloys there occurred complex structural changes depending on the HPT temperature and the concentration of vanadium x. The main features of these changes are as follows:

Feature 1. The lattice parameter of the fcc phase in RT-HPT and Cryo-HPT samples increases with increasing x and this trend is more pronounced in the RT-HPT samples.

Table 1. Structural characteristics, according to XRD investigations, of the fcc phase in HPT nanostructured CoCrFeMnNiV$_x$ alloys ($x = 0.2$, 0.5, 0.75), after RT-HPT and Cryo-HPT (torsional strain $\gamma \approx 80$).

Concentration of V ≡ x	Temperature HPT [K]	Lattice parameter [Å]	Texture degree $P_{(111)}$ [10^{-2}]	Crystallite size D [nm]	Microstrain $<\varepsilon>$ [10^{-3}]
0.2	77	3.600	64.8	14.1	1.66
0.5	77	3.604	63.1	11.9	1.85
0.75	77	3.609	64.6	18.2	2.75
0.2	300	3.598	57.7	18.9	1.73
0.5	300	3.606	60.6	18.5	1.76
0.75	300	3.615	63.9	18.0	2.89
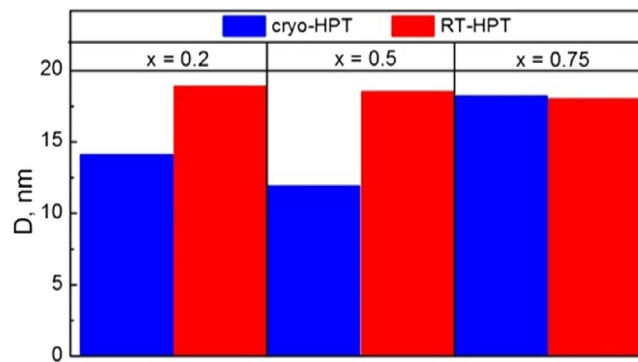
Figure 3. The value of the crystallite sizes D in the HPT nanostructured CoCrFeMnNiV$_x$ alloys after RT-HPT and Cryo-HPT (torsional strain $\gamma \approx 80$), for $x = 0.2$, 0.5, 0.75.
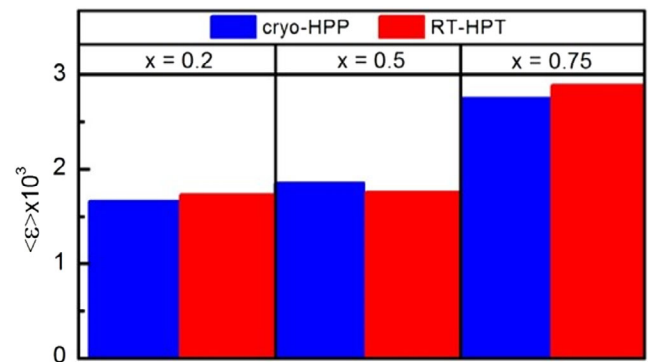
Figure 4. The microstrain $<\varepsilon>$ in the HPT nanostructured CoCrFeMnNiV$_x$ alloys after RT-HPT and Cryo-HPT (torsional strain $\gamma \approx 80$), for $x = 0.2$, 0.5, 0.75.

Feature 2. The value of $P_{(111)}$ characterizing the degree of sample texture changes slightly with increasing x both for Cryo-HPT samples (by less than 2.7%) and for RT-HPT samples (by about 11%). At the same time, $P_{(111)}$ in the Cryo-HPT samples is higher than in the RT-HPT samples for all values of x, with a maximum change of 12.3% observed at $x = 0.2$.

Feature 3. The D value in the RT-HPT samples is practically independent of x in the interval of $0.2 \leq x \leq 0.75$ (**Figure 3**). At the same time, another trend is observed for the Cryo-HPT samples such that, in the interval $0.2 \leq x \leq 0.5$, the value of D decreases by a factor of 1.18 and at $x = 0.75$ the value of D noticeably increases by a factor of about 1.5. Note that for $x \leq 0.5$ in the RT-HPT samples the D value is higher than in the Cryo-HPT samples by a factor of ≈ 1.6 at $x = 0.5$ while at $x = 0.75$ these values are almost the same (Figure 3). A minimum value of $D = 11.9$ nm is observed in the Cryo-HPT samples at $x = 0.5$.

Feature 4. The value $<\varepsilon>$ increases with x in the RT-HPT and in the Cryo-HPT samples. This dependence has two segments: at $x \leq 0.5$ the value of $<\varepsilon>$ slightly increases with x, but when x increases from 0.5 to 0.75 the value of $<\varepsilon>$ increases in the RT-HPT samples by ≈ 1.6 times and in the Cryo-HPT samples by ≈ 1.5 times (**Figure 4**).
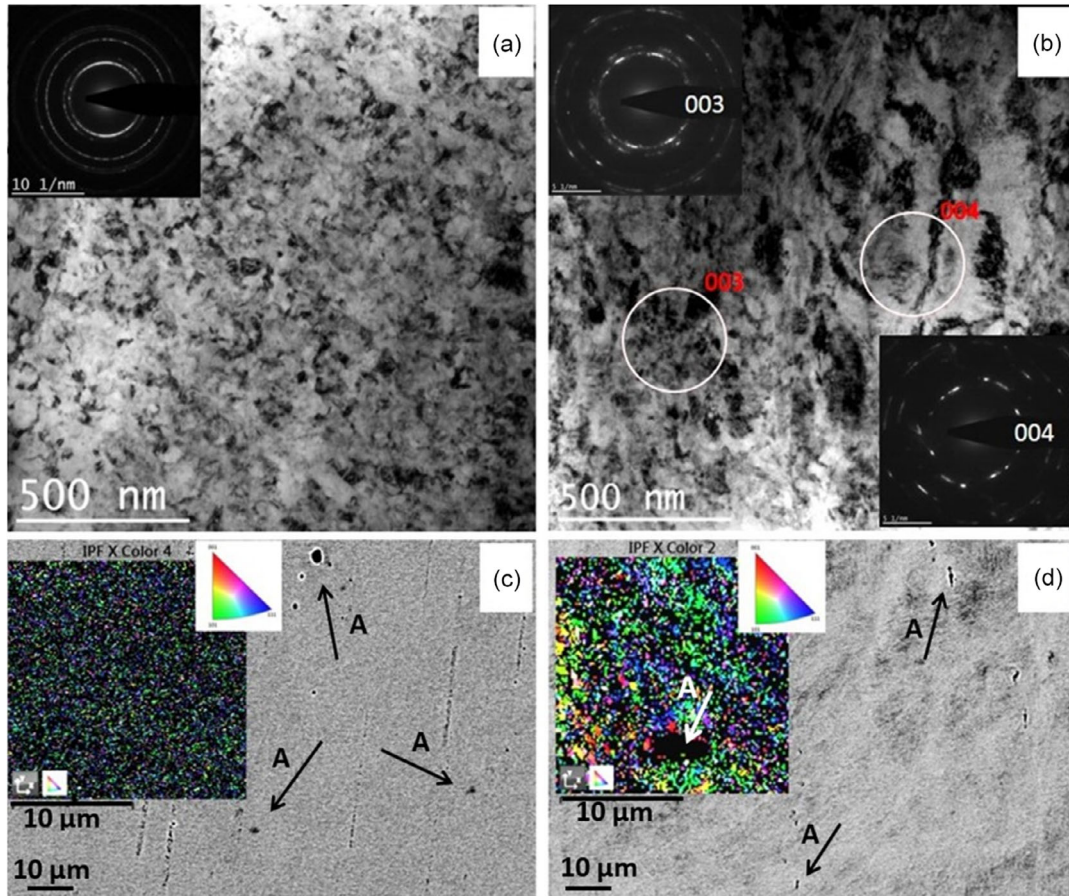
2.1.2. Electron Microscopy

The results of the Transmission Electron Microscopy (TEM) and Scanning Electron Microscopy (SEM) studies of the micro/

nanostructure of HEAs CoCrFeMnNiV$_{0.2}$ and CoCrFeMnNiV$_{0.75}$ samples after RT-HPT and Cryo-HPT for $\gamma \approx 80$ are shown in **Figure 5–8**.

After RT-HPT, the microstructure of the HPT nanostructured CoCrFeMnNiV$_{0.2}$ alloy (Figure 5a,c) comprised slightly elongated grains with a size ≈ 100 nm. By contrast, after Cryo-HPT an inhomogeneous structure was observed in the CoCrFeMnNiV$_{0.2}$ alloy. The TEM and electron backscatter diffraction images (Figure 5b,d) show both fine grains with a size of 50–100 nm randomly oriented (region 003 in Figure 5b) and regions with grains of ≈ 500–1000 nm in size (region 004 in Figure 5b); the latter show a clearly defined crystallographic orientation, as is evident by point reflections against the background of circular diffraction maxima (Figure 5b). Especially large grains have this predominant crystallographic orientation highlighted in green in Figure 5d. In addition, Figure 5d clearly demonstrates the inhomogeneity of the structure.

Also, in Figure 5c,d inclusions of μm and sub-μm sizes are visible (dark dots marked by arrow A); they were observed in almost all studies of the Cantor alloy and its analogues.[22–25] The characteristic appearance of these inclusions allows them to be classified as manganese oxides or more complex oxides.

The structural features of the HPT nanostructured CoCrFeMnNiV$_{0.2}$ sample after HTP at 77 K are presented in more detail in Figure 6. In Figure 6a, the electron diffraction pattern shown on the left side was taken from both areas 003 and 004 indicated in Figure 5b, i.e., representing an

ADVANCED
SCIENCE NEWS

www.advancedsciencenews.com

ADVANCED
ENGINEERING
MATERIALS

www.aem-journal.com

Figure 5. a,b) TEM images of the HPT nanostructured CoCrFeMnNiV$_{0.2}$ alloy with electron diffraction patterns (insets) and c,d) SEM images of the surface with orientational grain distribution maps (insets) obtained using EBSD: a,c) after RT-HPT and b,d) after Cryo-HPT, taken from areas of torsional strain $\gamma \approx 80$. Arrows A indicate oxide inclusions.
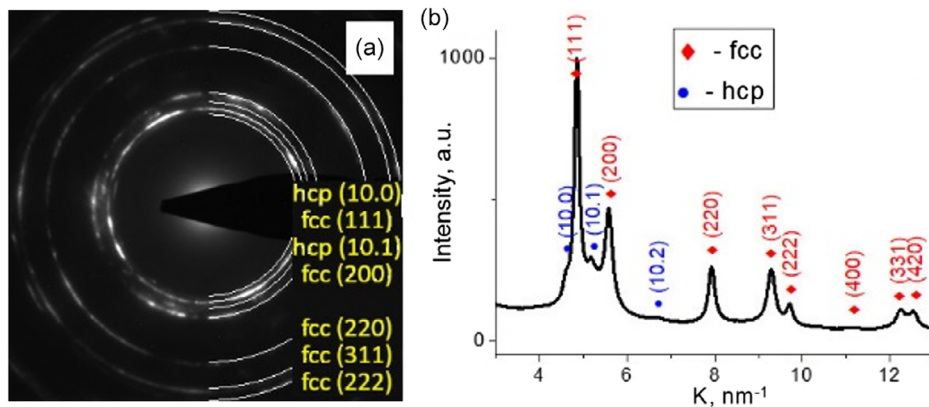
Figure 6. a) Electron diffraction pattern of the HPT nanostructured CoCrFeMnNiV$_{0.2}$ sample after Cryo-HPT (torsional strain $\gamma \approx 80$), taken from areas 003 and 004 (see Figure 5b). The phase-specific indices of reflections are given on the right half side of (a). b) Shows those reflections in terms of a diffraction intensity profile.

ultrafine/nanograined as well as CG microstructure, respectively; the right side of Figure 6a shows the result of indexing this diffraction pattern. As can be seen, in addition to reflections from the fcc in Figure 6b there are two additional reflections corresponding to interplanar distances $d = 2.167$ Å and 1.922 Å.

When calculating the diffraction intensity profiles, a third weak line was discovered (Figure 6b). It was established that these three lines belong to the hcp phase with lattice parameters $a = 2.51$ Å and $c = 4.14$ Å, whereas the lattice parameter of the fcc phase is $a = 3.57$ Å.
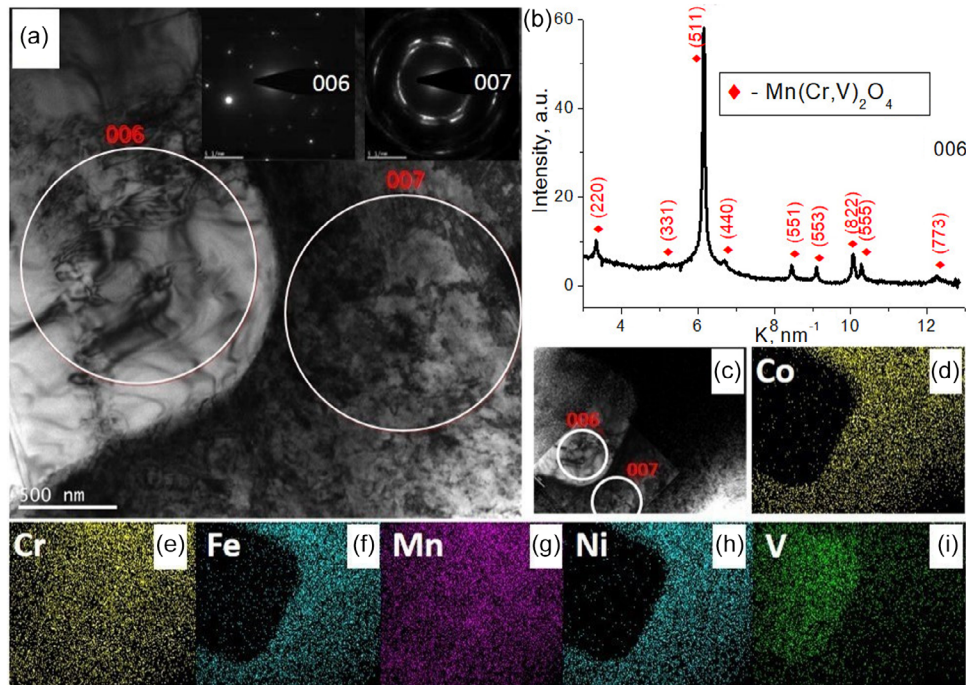
Figure 7. a,c) TEM images of the microstructure of the CoCrFeMnNiV$_{0.2}$ alloy in the Cryo-HPT sample (torsional strain $\gamma \approx 80$); b) diffraction intensity profiles of area 006, marked with a white circle in (a); and d–i) EDS maps of the distribution of the alloy components in areas 006 and 007 shown in (c).

Figure 7 shows the combined data on the microstructure of the CoCrFeMnNiV$_{0.2}$ alloy in the Cryo-HPT sample obtained using TEM images (Figure 7a,c), electron diffraction patterns (Figure 7b) of the 006 region marked with a white circle in Figure 7a,c, and energy diffraction spectroscopy (EDS) maps (Figure 7d–i) of the distribution of the alloy components in the regions 006 and 007 indicated in Figure 7c.

Analysis of Figure 7a,d–i shows that the area 006 in Figure 7a, c is part of the inclusion which in Figure 7d,f,h appears as a black spot, where this inclusion contains practically no cobalt, iron, and nickel. Chromium and manganese are almost evenly distributed between the matrix (area 007) and the inclusion (area 006) but the latter contains more vanadium than the matrix (Figure 7i). The matrix is in an HPT nanostructured state (Figure 7a, area 007), and all elements within it are evenly distributed (Figure 7d–i). When calculating the diffraction intensity profiles from area 006 (Figure 7b), it is apparent that the inclusion has an fcc lattice (spinel structure) with a lattice parameter $a = 8.44$ Å, and its composition can be described approximately as Mn(Cr,V)$_2$O$_4$.

Figure 8 shows the results of studying the microstructure of the HPT nanostructured alloy CoCrFeMnNiV$_{0.75}$ after both RT-HPT and Cryo-HPT. From the electron diffraction patterns (insets in Figure 8c,d), it follows that in both cases the structure consists of two phases: fcc and σ. The fcc phase after RT-HPT exhibits grain sizes between 40 and 100 nm (Figure 8a) while after Cryo-HPT, grains with sizes between 30 and 70 nm can be seen (Figure 8c). Also in case of the σ-phase, the microstructure after RT-HPT (Figure 8b) appears as a quite coarse one with particle sizes reaching 0.5 μm or more (Figure 8b) while the microstructure after Cryo-HPT (Figure 8d) is more refined. In both cases RT-HPT and Cryo-HPT, the heterogeneous character of microstructure is also demonstrated by the sizes of the phase regions fcc and σ which can reach several μm (see, e.g., Figure 8d).

2.2. Mechanical Characteristics of HPT Nanostructured CoCrFeMnNiV$_x$ Alloys
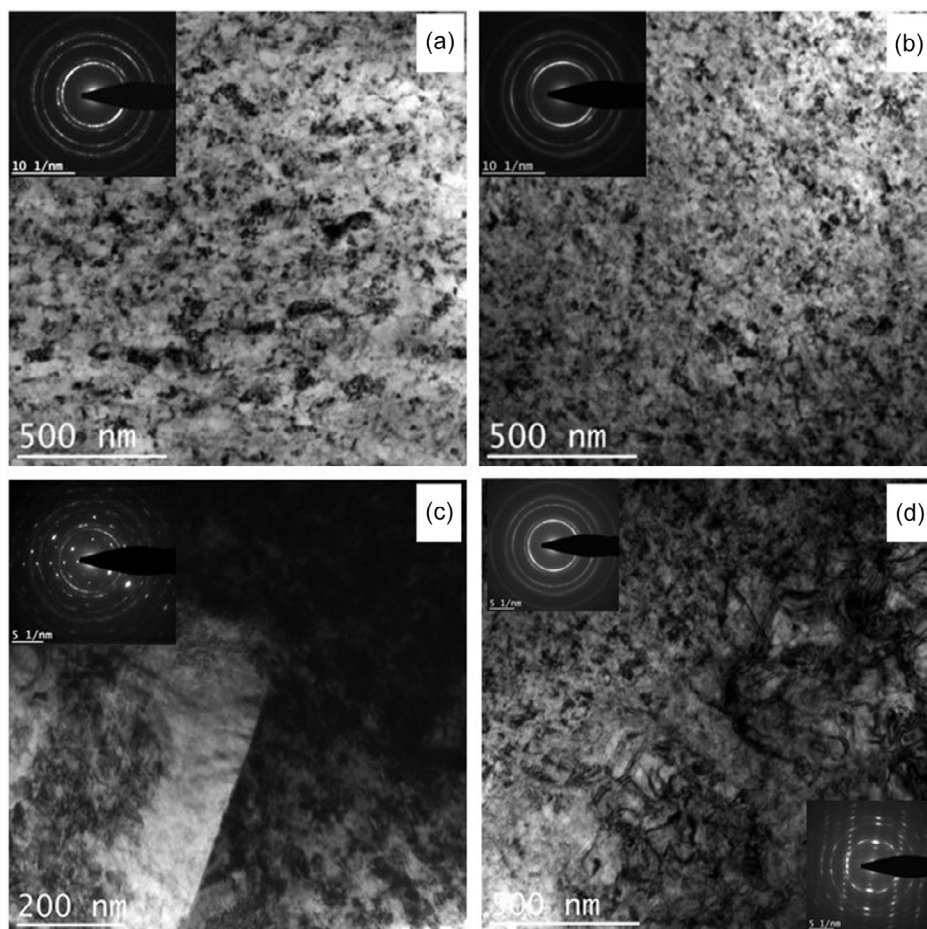
2.2.1. Torsional Shear Stress

Figure 9 shows the dependences of the shear stress τ measured in situ from shear strain γ in RT-HPT and Cryo-HPT for $x = 0.15$ and $x = 0.5$.

Figure 9 shows that during HPT deformation of the CoCrFeMnNiV$_{0.15}$ alloy at 300 K, the value of the shear stress τ for all γ (curve 2) is larger than the value of the shear stress τ during the HPT deformation at 77 K (curve 1). In the γ range from 80 to 180, the shear stress τ in curve 2 is ≈ 1.4 times larger than the corresponding shear stress τ in curve 1. For the CoCrFeMnNiV$_{0.5}$ alloy, the opposite effect is observed. During HPT at 300 K, the shear stress τ for all γ (curve 2) is smaller than the value of the shear stress τ during HPT at 77 K (curve 1). Thus, in the considered range of γ from 80 to 180, the shear stress τ on curve 2 is ≈ 1.3 times smaller than the corresponding shear stress τ on curve 1.

2.2.2. Microhardness

The measurements of microhardness H_v comprised those for the RT-HPT and Cryo-HPT samples (**Figure 10**) as a function of torsional strain γ and vanadium concentration x. They all are

ADVANCED
SCIENCE NEWS

www.advancedsciencenews.com

ADVANCED
ENGINEERING
MATERIALS

www.aem-journal.com

Figure 8. TEM images of HPT nanostructured CoCrFeMnNiV$_{0.75}$ alloy with electron diffraction patterns (insets) after a,c) RT-HPT and b,d) Cryo-HPT for areas with a torsional strain $\gamma \approx 80$. Images (a) and (b) were obtained from regions of the fcc phase and image (c) from a region with a tetragonal σ-phase. Image (d) was obtained from both the fcc phase (left upper area, with related diffraction pattern) and the tetragonal σ-phase (right bottom area, with related diffraction pattern).
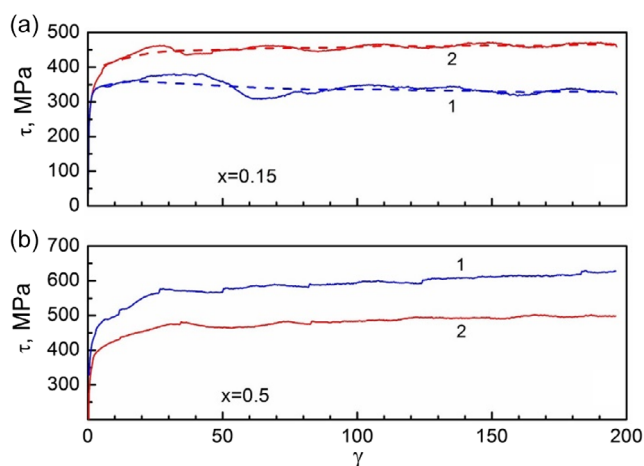
Figure 9. Dependences of the shear stress τ measured in situ on deformation γ in HPT processing for $x = 0.15$ (a) and $x = 0.5$ (b): curves 1, Cryo-HPT; curves 2, RT-HPT.

demonstrated in Figure 10a–e also including the values of $H_v(x)$ of the initial CG state (Figure 10f), taken from ref. [23]. It is important to note that the H_v dependences for $x = 0.2$, 0.3, and 0.5 shown in Figure 10b–d were measured both immediately after HPT and after exposure at room temperature for 48 h. It can be seen that for all γ the values of H_v practically did not change during the exposure time applied which indicates the general stability of the nanostructure in these alloys.

The observed concentration dependences of $H_v(\gamma)$ have a number of features. According to Figure 10, at $x \leq 0.3$ in the RT-HPT samples the H_v value is higher than in the Cryo-HPT samples, especially at torsional shear strains $\gamma \leq 80$. From $x \geq 0.5$ this difference changes to the opposite so that the H_v value in the RT-HPT samples becomes lower than in the Cryo-HPT samples. Figure 10 also shows that the $H_v(\gamma)$ dependences for different x differ from each other both for the Cryo-HPT and for the RT-HPT samples. In the region of small γ, the differences in H_v values of the Cryo-HPT and the RT-HPT samples for $x = 0.2$ and $x = 0.3$ are significantly larger than for the higher concentrations x. In the region of large γ, the differences of
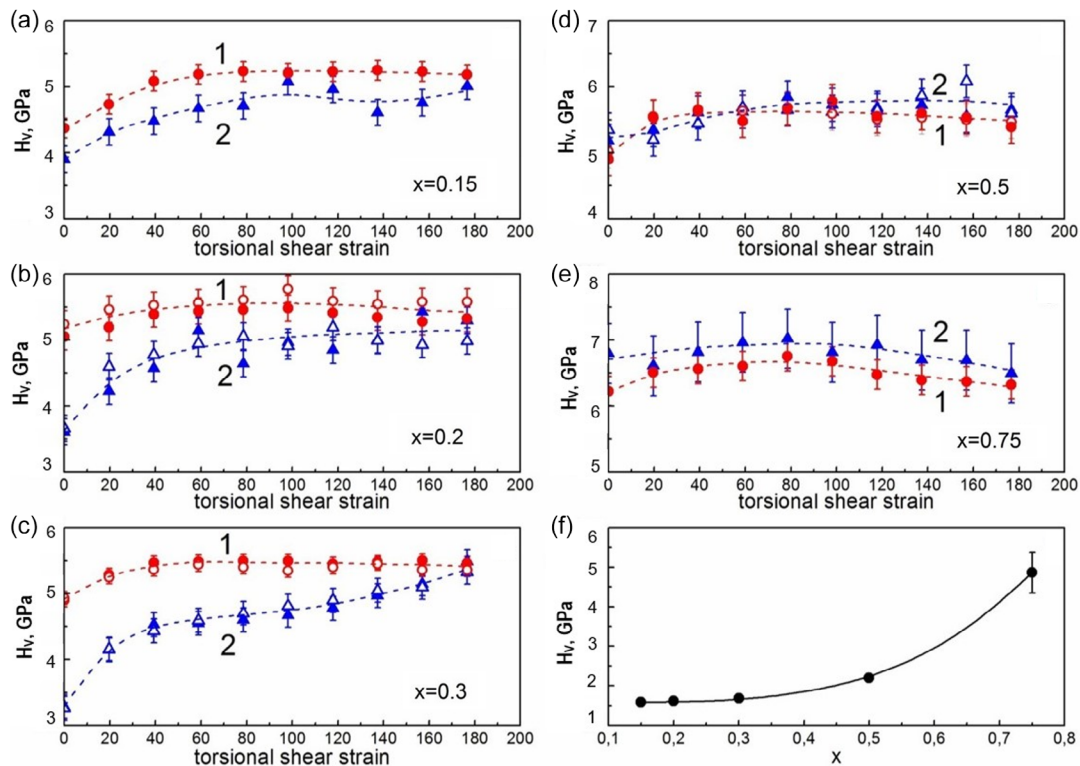
Figure 10. Dependences $H_v(\gamma)$ of HPT-nanostructured HEA CoCrFeMnNiV$_x$: a) for $x = 0.15$, b) for $x = 0.2$, c) for $x = 0.3$, d) for $x = 0.5$, and e) for $x = 0.75$. RT-HPT samplesare represented by curves 1 (a–e) Cryo-HPT samples by curves 2 (a–e). Figures (b–d) show the H_v values for $x = 0.2$, 0.3, and 0.5, respectively, measured immediately after HPT (curves 1(O), curves 2(△)) and after holding at room temperature for 48 h (curves 1(●), curves 2(▲)). Note that the first values in all graphs represent the H_v values from $0 < \gamma \leq 1$. f) The values of H_v ($\gamma = 0$) represent the initial CG state for different vanadium concentrations x.[23]

the $H_v(\gamma)$ dependences of the two sorts of samples are generally small. These effects can be also seen in **Figure 11**a,b which shows the concentration dependences of H_v of Figure 10 for the strains $\gamma \approx 80$ and $\gamma = 180$ of RT-HPT and Cryo-HPT samples in the form of histograms (the values of H_v at $\gamma \approx 180$ were obtained from areas $r \approx 4.5$, according to formula (1)). It can be seen that for both $\gamma \approx 80$ and $\gamma \approx 180$ the values of the microhardness H_v for all x in the HPT nanostructured state are significantly larger than in the CG state, but with increasing x these differences decrease. At shear strain $\gamma \approx 180$ (Figure 11b), the difference in the H_v values in the RT-HPT and Cryo-HPT samples is generally smaller. The reasons for this behavior will be discussed in Section 4.

It is important to note that for the alloys CoCrFeMnNiV$_{0.15}$ and CoCrFeMnNiV$_{0.5}$ the ratios of the shear stresses τ during HPT at 300 K and HPT at 77 K correlate with the corresponding ratios of H_v values for these alloys (for comments and conclusions from this finding, see Section 4.2).

2.2.3. Temperature Dependence of the Yield Strength $\sigma_{0.2}$

Figure 12 demonstrates the temperature dependences of the compression yield strength $\sigma_{0.2}(T)$ of the HPT nanostructured HEAs CoCrFeMnNiV$_{0.2}$ and CoCrFeNiMnV$_{0.5}$, both after processing by RT-HPT (curves 1) and by Cryo-HPT (curves 2).
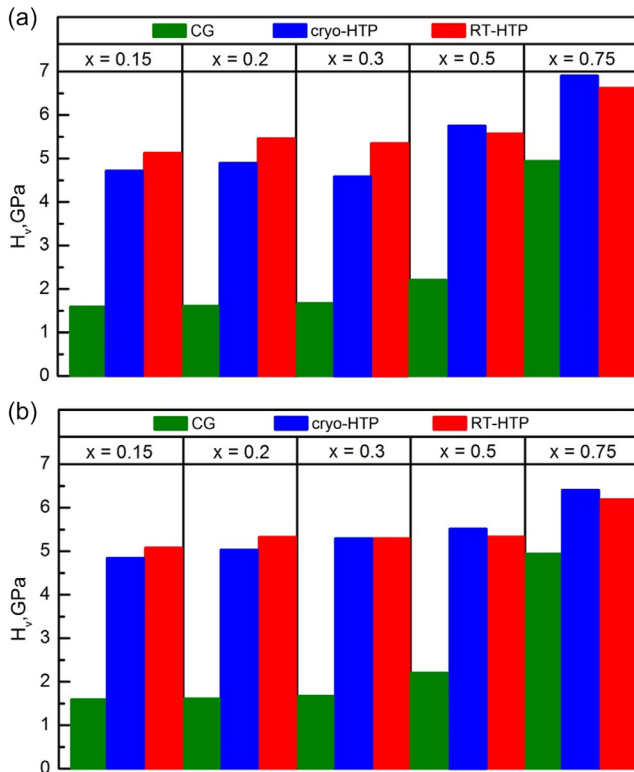
At first, when considering $\sigma_{0.2}$ values of CoCrFeMnNiV$_{0.2}$ alloy (Figure 12a), those of RT-HPT samples exceed the $\sigma_{0.2}$ values of Cryo-HPT samples throughout the entire temperature range. At the same time, in the CoCrFeMnNiV$_{0.5}$ alloy (Figure 12b), the values of $\sigma_{0.2}$ for RT-HPT samples are noticeably smaller than those in the Cryo-HPT samples.

Second, with the CoCrFeNiMnV$_{0.2}$ alloy, both the RT-HPT and the Cryo-HPT curve show a fairly linear increase of $\sigma_{0.2}$ with decreasing temperature from 300 down to 77 K. For the CoCrFeMnNiV$_{0.5}$ alloy, this linear increase of $\sigma_{0.2}$ holds only from 200 to 150 K; at lower temperatures, the $\sigma_{0.2}(T)$ dependences change character. In case of the CoCrFeMnNiV$_{0.2}$ alloy for temperatures below 20 K $\sigma_{0.2}$ decreases significantly, whereas in case of the CoCrFeMnNiV$_{0.5}$ alloy for temperatures below 150 K a levelling off toward 77 K occurs; for lower temperatures brittle failure occurred indicating the total loss of plasticity in this temperature range.

3. Discussion

3.1. Microstructure of HPT Alloys with Different Vanadium Concentrations

It is interesting to compare the structural parameters of alloys with different concentration of vanadium in the CG[22,23] and

**ADVANCED
SCIENCE NEWS**

www.advancedsciencenews.com

**ADVANCED
ENGINEERING
MATERIALS**

www.aem-journal.com

Figure 11. Microhardness H_v depending on x in the CoCrFeMnNiV$_x$ alloys in the CG and HPT nanostructured states, for samples after RT-HPT and Cryo- HPT, for a) $\gamma \approx 80$ and b) $\gamma \approx 180$. $H_v(x)$ data for CG states are taken from ref. [23].

Table 2. Lattice parameter a of fcc phase in CoCrFeMnNiV$_x$ alloys in different states. The measuring error amounts to ±0.002 in average.

| State	a [Å], $x = 0.2$	a [Å], $x = 0.25$	a [Å], $x = 0.5$	a [Å], $x = 0.75$
CG (after homogenization)[22]	–	3.594	3.601	3.604
HPT nanostructured (Cryo-HPT)	3.600	–	3.604	3.609
HPT nanostructured (RT-HPT)	3.598	–	3.606	3.615

HPT nanostructured states obtained by torsion under high pressure at 300 and 77 K (Table 1). It was shown earlier[23] that especially in the 1000 °C homogenized CG state, the lattice parameter a of the fcc phase increases with increasing concentration of vanadium (**Table 2**). The reason for this increase is the large atomic radius of dissolved vanadium atoms.[22,23] After carrying out HPT nanostructuring after annealing at 1000 °C, the trend of V-caused increase of lattice parameter (Table 2) is even larger, especially for the RT-HPT samples. While this effect can be explained by the increasing density of HPT-induced lattice

defects, the extraordinary increase of a of the RT-HPT samples may be attributed to the increased solubility limit (see, e.g., ref. [40]) in SPD-processed metals. Naturally, this increase is more likely in the case of RT-HPT deformation than at Cryo-HPT in which the equilibrium solubility limit and the diffusion mobility of atoms are significantly lower.

According to the TEM studies of the HPT nanostructured alloy CoCrFeMnNiV$_{0.2}$, there are obvious differences in the microstructure of the RT-HPT and Cryo-HPT samples (Figure 5). In the RT-HPT samples, a homogeneous microstructure with slightly elongated grains with a size of ≈100 nm is observed. By contrast, in the Cryo-HPT samples the microstructure is heterogeneous (Figure 5b,d): Together with small grains of the order of 50–100 nm, grains larger than 1 μm can be found (region 004 in Figure 5b). Similar differences in the microstructure of the RT-HPT and the Cryo-HPT samples were previously found for the HEAs CoCrFeMnNi[32] and Co$_{20}$Cr$_{26}$Fe$_{20}$Mn$_{20}$Ni$_{14}$.[36,37] In these works, it has been concluded that the reason for the development of an inhomogeneous microstructure in Cryo-HPT samples is the onset of deformation-induced martensitic transformation. As can be seen from Figure 5 and 6, in the Cryo-HPT samples of the HPT nanostructured CoCrFeMnNiV$_{0.2}$ alloy, very similar transformations occur, leading to the formation of microstructural areas with an increased grain size. Note that the lattice parameters of the martensitic hcp phase in the CoCrFeMnNiV$_{0.2}$ alloy are $a = 2.51$ nm and $c = 4.14$ nm, which, within the experimental error, agrees with the parameters obtained elsewhere for the Co$_{20}$Cr$_{26}$Fe$_{20}$Mn$_{20}$Ni$_{14}$ alloy.[37] Thus, the introduction of vanadium by an amount of concentration $x = 0.2$ does not suppress the martensitic transformation. Also in the Cantor alloy with
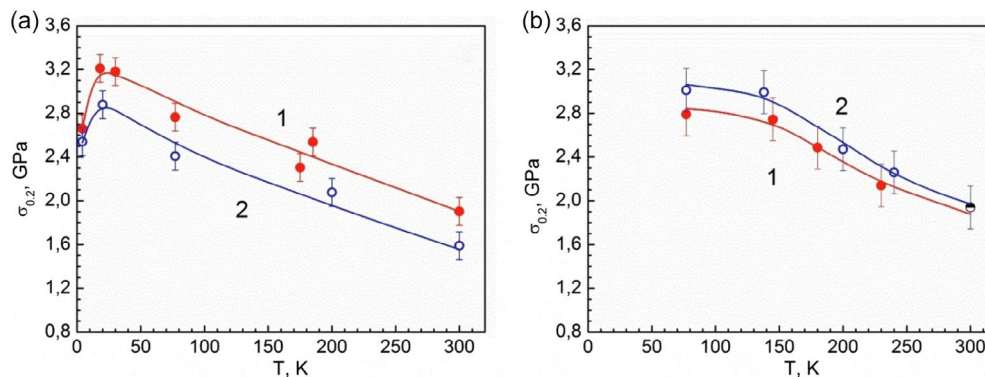
Figure 12. Temperature dependences of the yield strength $\sigma_{0.2}$ obtained under uniaxial compression at a constant strain rate of 3×10^{-4} s^{-1} for samples of alloys a) CoCrFeMnNiV$_{0.2}$ and b) CoCrFeMnNiV$_{0.5}$, after RT-HPT (curve 1) and Cryo-HPT (curve 2), torsional strain $\gamma \approx 80$.

$x = 0.3$, most of microhardness values of Cryo -HPT samples are lower than those o the RT- HPT samples (Figure 10c) which indicates the same mechanism to operate here (also compare the discussion in Section 3.2).

However, reaching $x = 0.5$ and especially $x = 0.75$, the CoCrFeNiMnV$_x$ alloy exhibits a new second phase both in the CG[22] and HPT nanostructured state (Figure 1). Besides the fcc grains, particles of the σ-phase are observed with volume fractions of 20% ($x = 0.5$) till 40–50% ($x = 0.75$). Note that the structure of the Cryo-HPT samples contains smaller grains of the fcc phase and smaller particles of the σ-phase each being compared to the RT-HPT samples (Figure 8).

3.2. Concentration Dependences of Microhardness, Torsional Stress, and Yield Strength

The correlation of microhardness values (Figure 10 and 11) with those of lattice parameter a (Table 2) is not too strong, neither for the CG nor the HPT nanostructured state. Especially the significant increase of the microhardness from vanadium concentrations $x = 0.5$ to $x = 0.75$ is not reflected by the increase of a which is practically linear in x, and the microhardness anomaly observed at low V concentrations $x \leq 0.3$ is not seen at all.

Considering the measured texture intensities of fcc phase (Table 1), also those do not seem to affect the microhardness data neither for different values of V concentration x nor for different HPT temperatures applied. The same is true for the value crystallite size D which is even smaller at Cryo-HPT than at RT-HPT (Figure 3) and therefore cannot account at all for the anomalous softening effect of Cryo-HPT. A similar situation is with the measured microstrains which show no difference between Cryo-HPT and RT-HPT (Figure 4), where the observed microhardness exhibits a marked difference. Only the strong increase of microstrains for samples with $x = 0.75$ (Table 1, Figure 4) correlates somewhat with the strong increase of microhardness both at Cryo-HPT and RT-HPT (Figure 11); this may be related with the appearance of the σ-phase especially at those high vanadium concentration.

Let us now consider the dependence of the microhardness on the vanadium concentration, x, of all the HPT nanostructured CoCrFeMnNiV$_x$ alloys obtained in this work (**Figure 13**), and compare them with the microhardness measurements for vanadium-free Cryo-HPT and RT-HPT CoCrFeMnNi ($x = 0$) alloy (the "Cantor" alloy) obtained earlier.[20,32,34] Concerning the dependence $H_v(x)$ for the RT-HPT samples, there are three distinct ranges (at $\gamma \approx 180$): at $x < 0.3$ the H_v value is higher in the RT-HPT samples than in the Cryo-HPT samples (called "anomalous behavior" in the following), while at $x > 0.3$ it is lower. At $x = 0.3$, the values of H_v for the RT-HPT and Cryo-HPT samples are similar. In what follows, we will discuss those ranges in detail in the next sections.

3.2.1. Vanadium Concentrations $x \leq 0.3$

In detail, we consider the alloys with concentrations $x = 0.15$–0.3 (Figure 10a–c) corresponding to single-phase alloys ($x = 0.15$ and $x = 0.2$), and an alloy with $x = 0.3$ which contains a small amount of σ-phase.[23] 1) At first, we emphasize that the "anomalous"
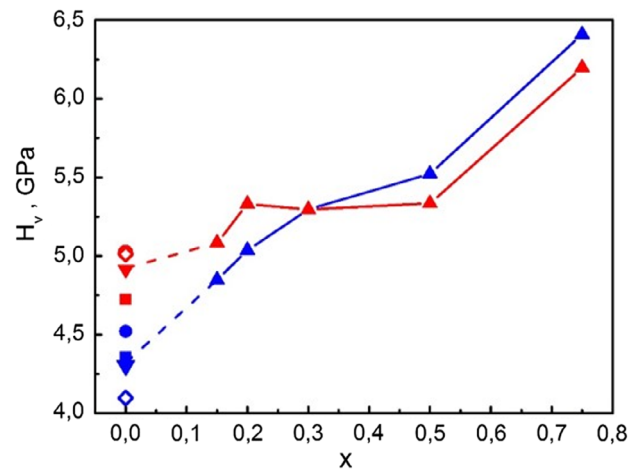
Figure 13. Dependences $H_v(x)$ of samples of HPT nanostructured HEA CoCrFeMnNiV$_x$ at $\gamma \approx 180$: ▲—RT-HPT; ▲—Cryo-HPT; ▼—RT-HPT;[32] ▼—Cryo-HPT;[32] ■—RT-HPT;[20] ■—Cryo-HPT;[20] ●—RT-HPT;[34] ●—Cryo-HPT;[34] ◇—RT-HPT;[35] and ◇—Cryo-HPT.[35]

behavior in the first range is also seen in the compression yield strength $\sigma_{0.2}$ of the CoCrFeMnNiV$_{0.2}$ alloy. Throughout the entire temperature range studied, the values of $\sigma_{0.2}$ in the Cryo-HPT samples are lower than in the RT-HPT samples (Figure 12a), in contrast to the values of $\sigma_{0.2}$ of undeformed CG samples where those measured at Cryo-temperature always exceed those measured at RT over the whole range of vanadium concentrations from $x = 0$ till $x = 0.75$.[25] 2) Second, we note that the microhardness values of samples with $x = 0.2$ and $x = 0.3$, when measured immediately after deformation and after 48 h, stay almost unchanged for each the Cryo-HPT and the RT-HPT samples which suggests that the microstructure formed in both cases is stable at room temperature (Figure 10b–d). Moreover, the significance of the "anomaly" is strongly confirmed by the torque values measured in situ during HPT deformation: The ratios of shear stresses $\tau(\gamma)$ of the Cryo-HPT and the RT-HPT samples (Figure 9a) well correlate with those of $H_v(\gamma)$ (Figure 10b,d). 3) Third and most important, a very similar behavior was found and reported for the CoCrFeMnNi alloy:[32,34,35] Also there, the observed changes in H_v were associated with changes in the microstructures formed during the RT-HPT and Cryo-HPT, showing an inhomogeneous microstructure in the Cryo-HPT samples caused by a partial martensitic transformation from the fcc to the hcp phase. 4) Fourth, when comparing the HPT-processed samples with $x = 0.15$, 0.2, and 0.3 at shear strains as small as $0 < \gamma \leq 1$, a marked difference is seen between the microhardness values of the Cryo-HPT and of the RT-HPT which increases with increasing x. For an alloy with $x = 0.15$, this difference is near 0.5 GPa and practically does not change with increasing γ up to $\gamma \approx 180$ (Figure 10a), like for the equiatomic Cantor alloy without vanadium.[32] For the alloys with $x = 0.2$ and $x = 0.3$, this difference is near 1.5–1.75 GPa but it decreases significantly with increasing γ (Figure 10b, c and 11). It may be assumed that in alloys with a vanadium concentration close to—or slightly exceeding—the solubility limit, the fcc lattice is in a metastable state. Already small deformations at liquid nitrogen temperature cause intense

phase transformation with the formation of an enlarged grain microstructure. However, with further deformation, grain fragmentation occurs and the microhardness of the Cryo-HPT and RT-HPT samples are brought closer together.

3.2.2. Vanadium Concentrations $x \geq 0.5$

Considering now the microhardness of Cryo-HPT and RT-HPT samples with concentrations $x \geq 0.5$, we see that the effect of grain fragmentation mentioned above keeps working till vanadium concentrations of $x = 0.5$, and the microhardness values of Cryo-HPT at $\gamma \approx 80$–180 start to exceed those of RT-HPT (Figure 10d and 11). The same behavior is observed in the values of $\sigma_{0.2}$ (Figure 12b). From that vanadium content $x = 0.5$ till the value $x = 0.75$, a permanent increase of both microhardness values of Cryo-HPT and of RT-HPT is observed (Figure 10f and 11a, b) which is in good correlation with the increase of volume fraction of σ-phase from about 20% to 40–50% see ref. [23]. Here, the increase of the H_v values of Cryo-HPT is stronger than those of the RT-HPT samples at all values of γ. This way, the anomaly which is observed at $x \leq 0.3$ has disappeared. This is an indirect evidence for the absence of martensitic transformation in HPT nanostructured alloys at $x > 0.3$. The fact that the Cryo-HPT samples exhibit both smaller particle sizes of the σ-phase and smaller grain sizes of the fcc phase (see Figure 8) explains that the related H_v values are higher than those of RT-HPT samples (Figure 11 and 13).

Also, the reversal/disappearance of the "anomaly" of H_v for vanadium concentrations $x \geq 0.5$ is strongly confirmed by the torque values measured in situ during HPT deformation (Figure 9b). Again, the ratios of shear stresses $\tau(\gamma)$ of the Cryo-HPT and the RT-HPT samples (Figure 9a) well correlate with those of $H_v(\gamma)$ (Figure 10b,d).

3.3. Low-Temperature Anomalies in the Temperature Dependences of the Yield Strength $\sigma_{0.2}$

It is apparent from Figure 12 that the value of $\sigma_{0.2}$ increases monotonically with decreasing temperature for the CoCrFeNiMnV$_{0.2}$ alloy in the temperature range of 25–300 K and for the CoCrFeMnNiV$_{0.5}$ alloy in the temperature range 150–300 K with a nearly linear slope. For the CoCrFeMnNiV$_{0.2}$ alloy, the average value of the derivative $d\sigma_{0.2}/dT$ is the same for all samples and is equal to ≈ 4.7 MPa/K. As is well known,[17] this type of temperature dependence of the yield strength is associated with the thermally activated nature of plastic deformation. In the alloys CoCrFeNiMnV$_{0.2}$ and CoCrFeMnNiV$_{0.5}$ in both the RT-HPT and Cryo-HPT samples, it can be seen in Figure 12 that, with decreasing temperature, this character of the dependence $\sigma_{0.2}(T)$ is violated. Thus, at $T < 20$ K as the temperature decreases in the CoCrFeMnNiV$_{0.2}$ alloy there is a decrease in $\sigma_{0.2}$ while in the CoCrFeNiMnV$_{0.5}$ alloy at $T < 150$ K the dependence $\sigma_{0.2}(T)$ shows a tendency toward the appearance of a plateau. Although there exist some recent reports investigations of HEAs concerning their mechanical properties and related mechanisms in the ultralow temperature regime,[41] no such unusual dependences $\sigma_{0.2}(T)$ in HEAs have been ever reported in the temperature ranges indicated.

Earlier, low-temperature anomalies were observed in CG HEAs (Al$_{0.5}$CoCrCuFeNi,[25] Fe$_{40}$Mn$_{40}$Co$_{10}$Cr$_{10}$,[42] and Fe$_{50}$Mn$_{30}$Co$_{10}$Cr$_{10}$[43]), but only for the range of ultralow temperatures (0.5–4.2 K). In these works, the anomalous behavior of $\sigma_{0.2}(T)$ was explained by a change in the mechanism of movement of dislocations from thermally activated to a quasidynamic inertial one, where local obstacles are overcome by dislocations without thermal activation. It should be noted that in the temperature range $T < 150$ K anomalous dependences of $\sigma_{0.2}(T)$ were also observed in some traditional metals and alloys,[44,45] in particular at temperatures $T < 25$ K in CG and nanostructured titanium.[46]

In the HPT nanostructured alloys CoCrFeMnNiV$_{0.2}$ and CoCrFeMnNiV$_{0.5}$ studied in the present work, the anomalous dependences of $\sigma_{0.2}(T)$ observed in the region of fairly high temperatures suggest to be explained in a similar way. In these HEAs, HPT achieved a strong fragmentation of grains and a large number of grain boundaries, and thus created nanostructures with short lengths of dislocation segments. These may be responsible for the fact that the mechanism of thermally inertial movement of dislocations is prevalent from the lowest up to unusually high temperatures before thermal activation governs the dislocation movement.

4. Summary and Conclusions

From the research works being reported in the current article, the following main findings result: 1) It has been established that in the alloy CoCrFeMnNiV$_x$ with $x < 0.5$ during HPT at a temperature of 77 K (pressure 6 GPa), the formation of a martensitic hcp phase occurs, as it has been previously reported for the Cantor alloy CoCrFeMnNi without the presence of vanadium. The lattice parameters of the hcp phase are $a = 2.51$ Å and $c = 4.14$ Å. As a result, a heterogeneous nanostructure is formed in the alloy, i.e., areas consisting of nanograins with sizes of 50–100 nm and areas with grains being as large as 0.5–1 μm. The alloy also contained a few inclusions of spinel-type oxides Mn(Cr,V)$_2$O$_4$ of μm to sub-μm sizes exhibiting a lattice parameter of $a = 8.44$ Å. 2) For $x \geq 0.5$, another dispersed two-phase microstructure develops during both Cryo-HPT and RT-HPT, which now consists of the fcc phase and the tetragonal σ-phase. This microstructure is more finely dispersed after Cryo-HPT than after RT-HPT. 3) In correspondence to the features of HPT nanostructures, a contrary dependence of the microhardness value on the HPT temperature was established in alloys with different x values. This dependence has been fully confirmed by in situ torque measurements during HPT processing. At small values of x ($x = 0.15$, 0.2, and 0.3) after Cryo-HPT, anomalous softening of the alloy was observed so that the H_v value in Cryo-HPT samples was smaller than in the RT-HPT samples. This is the result of a martensitic transformation during low-temperature deformation, leading to the formation of regions with a coarser grain structure. It has been shown that this nanostructure is time-stable, at least for 48 h. At $x \geq 0.5$, the opposite effect was observed so that the H_v value in the Cryo-HPT samples is larger than in the RT-HPT samples. This effect is due to the formation of a finer two-phase microstructure, consisting of nanograins of the plastic fcc phase and particles of the brittle σ-phase with a very high hardness. 4) In the temperature range

4.2–300 K in the CoCrFeNiMnV$_{0.2}$ alloy, the values of compression yield stress $\sigma_{0.2}$ for RT-HPT samples exceed those for Cryo-HPT samples. In the CoCrFeMnNiV$_{0.5}$ alloy, the opposite effect was observed: the values of $\sigma_{0.2}$ for RT-HPT samples are smaller than those for Cryo-HPT samples. The ratios of $\sigma_{0.2}$ values in RT-HPT and Cryo-HPT samples for the CoCrFeMnNiV$_{0.2}$ and CoCrFeMnNiV$_{0.5}$ alloys correlate with the ratios of $H_v(\gamma)$ values and shear stress values $\tau(\gamma)$ for these alloys. 5) It has been established that during active compression of samples of both RT-HPT and Cryo-HPT in HPT nanostructured alloys CoCrFeMnNiV$_{0.2}$ (in the temperature range 20–300 K) and in HPT nanostructured alloys CoCrFeMnNiV$_{0.5}$ (in the temperature range 150–300 K), thermally activated plastic deformation occurs. However, for the first time in HEAs, anomalous dependences of $\sigma_{0.2}(T)$ were observed at temperatures 4.2–20 K for the CoCrFeMnNiV$_{0.2}$ HEA and 80–150 K for CoCrFeMnNiV$_{0.5}$ HEA. Severely fragmented grains and a high density of grain boundaries in these HPT nanostructured HEAs seem to achieve non-thermal inertial dislocation movement in these cases.

5. Experimental Section

Alloys of CoCrFeMnNiV$_x$ ($x = 0.15$, 0.2, 0.3, 0.5, 0.75 which is 2.91, 3.85, 5.66, 9.09, and 13.04 at% vanadium, respectively) were received by arc melting of high purity elements in an atmosphere of high-purity argon inside water-cooled copper cavities. The purity of the alloying elements was beyond 99.9 at%. To ensure chemical homogeneity, the ingots were turned over and remelted at least five times. Thereafter, homogenization annealing was carried out at 1000 °C for 24 h in an evacuated quartz ampoule. The resulting workpieces of the CoCrFeMnNiV$_x$ alloys ($x = 0.15$, 0.2, 0.3, 0.5), 5.3 mm thick, were cold-rolled to a thickness of 2 mm and subjected to intermediate annealing at a temperature of 800 °C for 1 h. The resulting tapes were cold-rolled to a thickness of 1 mm and annealed again at a temperature of 1000 °C for 1 h in an atmosphere of high-purity argon. The average grain size after such treatment was $\approx 4 \mu m$ where this is designated the initial CG state. Discs with diameters of 10 mm were cut from the resulting tapes and both sides were ground to a thickness of 0.9 mm. Due to its high fragility, it was not possible to roll the CoCrFeNiMnV$_{0.75}$ alloy, and therefore the disks were cut by spark erosion directly from the ingot. Then they underwent the same annealing and grinding procedure as the discs of the other compositions. The discs were subjected to severe plastic deformation using a HPT facility built by KLEMENT, Austria using Bridgman-type anvils described in detail earlier.[32] The HPT deformation was carried out at temperatures of 300 K (RT-HPT samples) and 77 K (Cryo-HPT samples) under a quasihydrostatic pressure of 6 GPa, a fixed number of revolutions $n = 5$, and a fixed final thickness of the discs of $h \approx 0.8$ mm. The HPT shear strain γ was determined using the relationship

$$\gamma = 2\pi n r / h \tag{1}$$

As parameters n and h were kept constant throughout this work, γ only depends on the distance r from the rotation axis to the site of area observed.

The temperature of 77 K during HPT was obtained by immersing the sample and plungers in liquid nitrogen. The plungers were rotated at a speed of 0.2 rpm which corresponded to a maximum shear strain rate during torsion of $d\gamma/dt = 0.11$ s^{-1}. There was no slippage of the plungers relative to the surface of the samples during HPT processing.[32,38] During the HPT process, the torques Q were measured and the corresponding shear stresses τ were evaluated at an accuracy of ≈ 1 MPa, by means of the equation

$$\tau = 3Q/(2\pi R^3) \tag{2}$$

where Q is the torque and R is the radius of the HPT disk.

The X-ray diffraction (XRD) analysis was carried out on a DRON-4-07 diffractometer in a filtered Cu Kα radiation ($\lambda = 0.154187$ nm). For the estimation of microstructural characteristics of samples (crystallites size and microstrains), the Williamson–Hall method[39] was applied. Here, the true physical broadening of Bragg peaks β is given by

$$\beta = \frac{\lambda}{D\cos(\theta)} + 4 \ <\varepsilon> \ \mathrm{tg}(\theta) \tag{3}$$

where λ is the X-ray wavelength, D is the crystallite size (size of coherent scattering domains), $<\varepsilon>$ is the microstrain, and θ is the diffraction angle. The instrumental function was obtained from a reference sample of recrystallized silicon powder with a particle size of $\approx 30 \mu m$.

The microstructure of samples after HPT processing was studied using a PHILIPS CM200 transmission electron microscope (TEM) with disks electropolished and thinned using an electrolyte consisting of 95% C$_2$H$_5$OH and 5% HClO$_4$. Using selected area diffraction, electron diffraction patterns from sample areas as small as 1.2 μm were achieved. The diffraction intensity profiles were calculated by integration along the diffraction rings using the PASAD tools.[32] Samples for scanning electron microscopy (SEM) were ground by SiC papers with 600 and 1200 grit and then polished using Al$_2$O$_3$ powders with particle sizes of 1 and 0.3 μm. The polished surfaces were investigated in the back-scattered polished surfaces on an FEG-SEM ZEISS SUPRA 55 V microscope.

Disks were mechanically polished before taking microhardness measurements. The Vickers microhardness H_v was measured in samples after HPT at a temperature of 300 K—immediately after HPT and after exposure for 48 h under ambient conditions. For these measurements, a load of 1.5 N was applied for 15 s. The indentations were made at a distance of 0.5 mm from each other in a direction from the center of the disk to the edge along four different radial directions. These four values were averaged and plotted on the relevant graphs. After HPT, samples were cut from the discs for uniaxial compression testing with dimensions of $0.8 \times 0.8 \times 1.3$ mm^3. These tests were performed with a strain rate of 3×10^{-4} s^{-1} using an MRK-3 deformation testing machine at an ambient temperature of 290 K or at cryogenic temperatures using liquid and gaseous nitrogen and helium.

Conflict of Interest

The authors declare no conflict of interest.

Data Availability Statement

The data that support the findings of this study are available from the corresponding author upon reasonable request.

Keywords

ADVANCED
SCIENCE NEWS

www.advancedsciencenews.com

ADVANCED
ENGINEERING
MATERIALS

www.aem-journal.com

[1] J.-W. Yeh, S.-K. Chen, S.-J. Lin, J.-Y. Gan, T.-S. Chin, T.-T. Shun, C.-H. Tsau, S.-Y. Chang, *Adv. Eng. Mater.* **2004**, *6*, 299.

[2] B. Cantor, I. T. H. Chang, P. Knight, A. J. B. Vincent, *Mater. Sci. Eng. A* **2004**, *375*, 213.

[3] Y. Zhang, T. T. Zuo, Z. Tang, M. C. Gao, K. A. Dahmen, P. K. Liaw, Z. P. Lu, *Prog. Mater. Sci.* **2014**, *61*, 1.

[4] W. Skrotzki, R. Chulist, *Mater. Trans.* **2023**, *64*, 1769.

[5] M. A. Laktionova, E. D. Tabchnikova, Z. Tang, P. K. Liaw, *Low Temp. Phys.* **2013**, *39*, 630.

[6] J. Moon, E. Tabachnikova, S. Shumilin, T. Hryhorova, Y. Estrin, J. Brechtl, P. Liaw, W. Wang, K. A. Dahmen, H. S. Kim, *Phys. Rev. Mater.* **2021**, *5*, 083601.

[7] B. Schuh, F. Mendez-Martin, B. Völker, E. P. George, H. Clemens, R. Pippan, A. Hohenwarter, *Acta Mater.* **2015**, *96*, 258.

[8] D. H. Lee, I. C. Choi, M. Y. Seok, J. He, Z. Lu, J.-Y. Suh, M. Kawasaki, T. G. Langdon, *J. Mater. Res.* **2015**, *30*, 2804.

[9] A. Heczel, M. Kawasaki, J. L. Lábár, *J. Alloys Compd.* **2017**, *711*, 143.

[10] G. Laplanche, A. Kostka, O. M. Horst, G. Eggeler, E. P. George, *Acta Mater.* **2016**, *118*, 152.

[11] A. S. Tirunilai, T. Hanemann, C. Reinhart, V. Tschan, K.-P. Weiss, G. Laplanche, J. Freudenberger, *Mater. Sci. Eng. A.* **2020**, *783*, 139290.

[12] F. Otto, N. L. Hanold, E. P. George, *Intermetallics* **2014**, *54*, 39.

[13] S. Chen, H. S. Oh, B. Gludovatz, S. J. Kim, E. S. Park, Z. Zhang, R. O. Ritchie, Q. Yu, *Nat. Commun.* **2020**, *11*, 826.

[14] B. Gludovatz, R. O. Ritchie, *MRS Bull.* **2022**, *47*, 176.

[15] E. Tabachnikova, T. Hryhorova, S. Shumilin, Y. Semerenko, Y. Huang, T. Langdon, *Mater. Trans.* **2023**, *64*, 1806.

[16] S. Zherebtsov, N. Stepanov, Y. Ivanisenko, D. Shaysultanov, N. Yurchenko, M. Klimova, G. Salishchev, *Metals* **2018**, *8*, 123.

[17] A. V. Podolskiy, E. Schafler, E. D. Tabachnikova, M. A. Tikhonovsky, M. J. Zehetbauer, *Low Temp. Phys.* **2018**, *44*, 976.

[18] H. Shahmir, M. S. Mehranpour, S. A. A. Shams, T. G. Langdon, *J. Mater. Res. Technol.* **2023**, *23*, 3362.

[19] D.-H. Lee, J.-A. Lee, Y. Zhao, Z. Lu, J.-Y. Suh, J.-Y. Kim, U. Ramamurty, M. Kawasaki, T. G. Langdon, *Acta Mater.* **2017**, *140*, 443.

[20] H. V. Rusakova, L. S. Fomenko, S. N. Smirnov, A. V. Podolskiy, Y. O. Shapovalov, E. D. Tabachnikova, M. A. Tikhonovsky, A. V. Levenets, M. J. Zehetbauer, E. Schafler, *Mater. Sci. Eng. A* **2021**, *828*, 142116.

[21] E. D. Tabachnikova, M. A. Laktionova, Yu. A. Semerenko, S. E. Shumilin, A. V. Podolskiy, M. A. Tikhonovsky, J. Miskuf, K. Csach, *Low Temp. Phys.* **2017**, *43*, 1108.

[22] G. A. Salishchev, M. A. Tikhonovsky, D. G. Shaysultanov, N. D. Stepanov, A. V. Kuznetsov, I. V. Kolodiy, A. S. Tortika, O. N. Senkov, *J. Alloys Compd.* **2014**, *591*, 11.

[23] N. D. Stepanov, D. G. Shaysultanov, G. A. Salishchev, M. A. Tikhonovsky, E. E. Oleynik, A. S. Tortika, O. N. Senkov, *J. Alloys Compd.* **2015**, *628*, 170.

[24] A. Radi, C. S. V. Seyedmohammadi, H. S. Kim, G. G. Yapic, *J. Alloys Compd.* **2023**, *968*, 172093.

[25] E.D. Tabachnikova, A.V. Podolskiy, M. O. Laktionova, N. A. Bereznaia, M. A. Tikhonovsky, A. S. Tortika, *J. Alloys Compd.* **2017**, *698*, 501.

[26] H. Shahmir, M. Nili-Ahmadabadi, A. Shafiee, T. G. Langdon, *Mater. Sci. Eng. A* **2018**, *718*, 468.

[27] H. Shahmir, E. Tabachnikova, A. Podolskiy, M. Tikhonovsky, T. G. Langdon, *J. Mater. Sci.* **2018**, *53*, 11813.

[28] X. Liu, H. Ding, Y. Huang, X. Bai, Q. Zhang, H. Zhang, T. G. Langdon, J. Cui, *J. Alloys Compd.* **2021**, *867*, 159063.

[29] R. B. Figueiredo, W. Wolf, T. G. Langdon, *J. Mater. Res. Technol.* **2022**, *20*, 2358.

[30] K. Edalati, J. M. Cubero-Sesin, A. Alhamidi, I. F. Mohamed, Z. Horita, *Mater. Sci. Eng. A* **2014**, *613*, 103.

[31] A. V. Podolskiy, C. Mangler, E. Schafler, E. D. Tabachnikova, M. J. Zehetbauer, *J. Mater. Sci.* **2013**, *48*, 4689.

[32] A. V. Podolskiy, Y. O. Shapovalov, E. D. Tabachnikova, A. S. Tortika, M. A. Tikhonovsky, B. Joni, E. Ódor, T. Ungar, S. Maier, C. Rentenberger, M. J. Zehetbauer, E. Schafler, *Adv. Eng. Mater.* **2020**, *22*, 1900752.

[33] Y. O. Shapovalov, E. D. Tabachnikova, M. A. Tikhonovsky, A. V. Levenets, M. J. Zehetbauer, E. Schafler, *J. V.N. Karazin Kh. Nat. Univ. Phys.* **2020**, *32*, 59.

[34] W. Skrotzki, A. Pukenas, E. Odor, B. Joni, T. Ungar, B. Völker, A. Hohenwarter, R. Pippan, E.-P. George, *Crystals* **2020**, *10*, 336.

[35] R. Chulist, A. Pukenas, P. Chekhonin, A. Hohenwarter, R. Pippan, N. Schell, W. Skrotzki, *Materials* **2022**, *15*, 8407.

[36] J. Moon, Y. Qi, E. Tabachnikova, *Mater. Lett.* **2017**, *202*, 86.

[37] J. Moon, Y. Qi, E. Tabachnikova, *Sci. Rep.* **2018**, *8*, 11074.

[38] K. Edalati, Z. Horita, T. G. Langdon, *Scr. Mater.* **2009**, *60*, 9.

[39] G. K. Williamson, W. H. Hall, *Acta Metall.* **1953**, *1*, 22.

[40] V. N. Voyevodin, M. A. Tikhonovsky, *Mater. Sci. Eng. A* **2021**, *822*, 141686.

[41] M. Naeem, H. He, F. Zhang, H. Huang, S. Harjo, T. Kawasaki, B. Wang, S. Lan, Z. Wu, F. Wang, Y. Wu, Z. Lu, Z. Zhang, C. T. Liu, X.-L. Wang, *Sci. Adv.* **2020**, *6*, eaax4002.

[42] T. V. Hryhorova, S. E. Shumilin, Y. O. Shapovalov, Y. O. Semerenko, O. D. Tabachnikova, M. A. Tikhonovsky, A. S. Tortika, M. J. Zehetbauer, E. Schafler, *J. V. N. Karazin Kh. Nat. Univ. Phys.* **2020**, *32*, 41.

[43] E. D. Tabachnikova, T. V. Hryhorova, S. E. Shumilin, I. V. Kolodiy, *Low Temp. Phys.* **2022**, *48*, 1108.

[44] V. V. Pustovalov, *Low Temp. Phys.* **2000**, *26*, 375.

[45] *Plastic Deformation of Crystals at Low Temperatures*, Naukova Dumka, Kyiv **2012**.

[46] V. A. Moskalenko, R. V. Smolianets, V. D. Natsik, *Low Temp. Phys.* **2023**, *49*, 248.